Robustness of the scalar elastic imaging condition for converted waves

Yuting Duan & Paul Sava
Center for Wave Phenomena, Colorado School of Mines

ABSTRACT
For elastic reverse-time migration, one constructs elastic source and receiver wavefields using a source function and multi-component data, and then applies an imaging condition to the reconstructed wavefields. A widely used imaging condition is cross-correlation of individual wave modes separated in both wavefields, e.g., compressional (P) waves and shear (S) waves. One difficulty in elastic migration is that the PS and SP images change sign at normal incidence. We recently proposed a scalar imaging condition that corrects for the polarity change; however, this imaging condition requires additional prior information, specifically the reflector normal. Here, we address two practical issues associated with this imaging condition. The first is the estimation of the reflector normal. Using incorrect P- and S-mode velocities causes reflectors in migrated PP, PS, and SP images to be shifted from their true positions. We show that it is more reliable to estimate reflector normals from PS and SP images, computed using conventional imaging methods, instead of from PP images. The second issue is the illumination and imaging of a reflector from its opposite sides. We demonstrate that the PS and SP images computed using waves from opposite sides of a reflector have the same polarity, and therefore they can be stacked over experiments without canceling each other at various positions in space. Several numerical examples illustrate the two issues in simple and complex models.

Key words: elastic migration, scalar imaging condition

1 INTRODUCTION

Conventional seismic data processing is typically based on the acoustic wave equation, and thus uses only compressional waves while regarding shear waves as noise. While this simplification is useful in practice, it may lead to incorrect geologic model reconstruction and incomplete reservoir characterizations. Ongoing improvements in computational capability and seismic acquisition have made imaging using multi-component elastic waves feasible. Multi-component seismic data can provide additional subsurface information, such as that regarding fracture distributions and elastic properties (MacLeod et al., 1999; Mehta et al., 2009; Sen, 2009).

In elastic reverse-time migration, wavefield extrapolation reconstructs vector source and receiver wavefields. Multi-component elastic wavefields allow for a variety of imaging conditions (Yan and Sava, 2008; Denli and Huang, 2008; Artman et al., 2009; Wu et al., 2010; Duan and Sava, 2014). One widely used imaging condition is crosscorrelation of separated wave modes in source and receiver wavefields, which yields PP, PS, SP, and SS images. However, because PS and SP reflectivities change signs at certain incidence angles, PS and SP images computed using this imaging condition change polarities at the corresponding angles.

Duan and Sava (2014) propose an imaging condition for elastic reverse-time migration, generating PS and SP scalar images with consistent polarity information for various experiments. This imaging condition requires additional information that is not available in the extrapolated wavefield, specifically the reflector normal field. In this paper, we investigate two practical problems associated with this imaging condition, including the estimation of the reflector normals when the reflectors are imaged at incorrect positions, and the imaging of a reflector by waves from opposite sides.

2 ELASTIC SCALAR IMAGING CONDITION

Reconstructed source and receiver wavefields typically are decomposed into P- and S-modes prior to application of an imaging condition (Dellinger and Etgen, 1990; Yan and Sava, 2008). In isotropic media, a widely used method for P- and S-mode separation is the Helmholtz decomposition (Aki and Richards, 2002). By computing the divergence and curl of the

displacement wavefield, we obtain the P- and S-modes:

$$P = \nabla \cdot \mathbf{u} \,, \tag{1}$$

$$\mathbf{S} = \nabla \times \mathbf{u} \,. \tag{2}$$

Here, $P(e, \mathbf{x}, t)$ and $\mathbf{S}(e, \mathbf{x}, t)$ are functions of the experiment index e, space coordinate $\mathbf{x} = \{x, y, z\}$, and time t, and they represent the scalar P- and vector S-modes after Helmholtz decomposition, respectively.

A direct approach for computing PS and SP images is to crosscorrelate the corresponding modes in source and receiver wavefields (Yan and Sava, 2008), hereby referred to as the conventional imaging condition. Duan and Sava (2014) propose alternative imaging conditions that result in scalar PS and SP images:

$$I^{PS} = \sum_{e,t} (\nabla P \times \mathbf{n}) \cdot \mathbf{S} \,, \tag{3}$$

$$I^{SP} = \sum_{e,t} (\nabla \times \mathbf{S} \cdot \mathbf{n}) \, P \,. \tag{4}$$

The PS and SP scalar images are denoted by $I^{PS}(\mathbf{x})$ and $I^{SP}(\mathbf{x})$, respectively, and vector $\mathbf{n}(\mathbf{x})$ is a unit vector specifying the reflector normal and is assumed as prior information. This imaging condition is referred to as the scalar imaging condition.

For the PS imaging condition (equation 3), vector ∇P is parallel to the propagation direction of the incident P-mode, as seen in Figure 1. The cross product of ∇P and normal vector $\mathbf{n}$ forms a vector orthogonal to the reflection plane $\mathcal{R}$, but parallel to vector $\mathbf{S}$, which is the polarization direction of the reflected S-mode. There is a similar physical interpretation for the SP imaging condition (equation 4). The curl of vector $\mathbf{S}$ is within plane $\mathcal{R}$, and the dot product of $\nabla \times \mathbf{S}$ and the normal vector $\mathbf{n}$ forms a scalar field that characterizes the magnitude of the S-mode. We can simply correlate this quantity with the scalar reflected P wavefield. When the incidence angle changes sign, and the reflected P- and S-modes consequently change sign, vectors $\nabla P \times \mathbf{n}$ and $\nabla \times \mathbf{S}$ reverse direction, thus compensating for the opposite polarization of the reflected P- and S-modes, respectively. Therefore, using this imaging condition, we are able to obtain PS and SP images without polarity reversal.

We illustrate the imaging condition with a 2D synthetic model, which contains one horizontal reflector at $z = 0.5$ km, Figure 2(a). A displacement source is at $(0.75, 0.05)$ km and the source function is a Ricker wavelet with a peak frequency of 30 Hz. A receiver line is at depth $z = 0.15$ km. By crosscorrelating the P modes in source and receiver wavefields, we obtain the PP image, Figure 2(b). Using the scalar imaging condition, we obtain PS and SP images, shown in Figures 2(c) and 2(d). In PS and SP images, there is no polarity reversal, which allows us to stack multiple elastic images over experiments. In this case, we estimate the reflector normal $\mathbf{n}$ for migration from the PP image, and we use correct P- and S-velocity models for migration.

However, in practice, it is not realistic to obtain the true model, and the reflectors may be imaged at various positions in PP, PS, and SP images. In the following section, we show a robust way to estimate the reflector normal for imaging converted wave-modes.

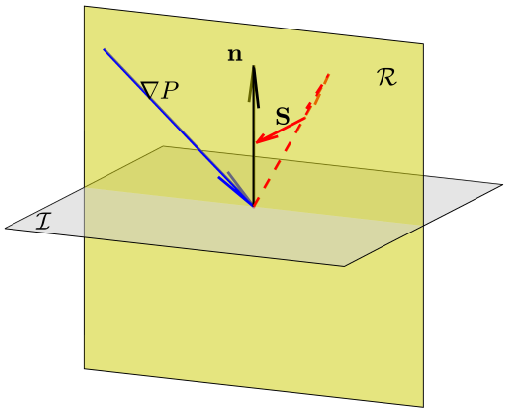
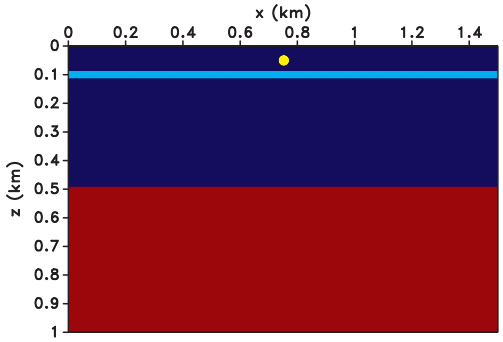


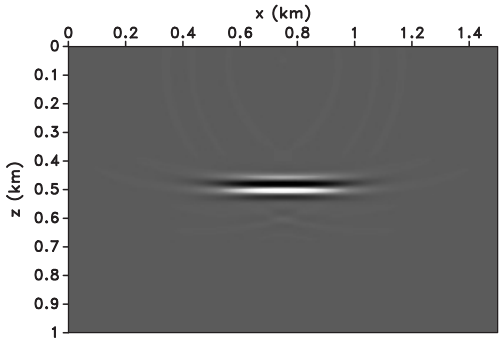
Figure 1. Schematic representation of reflection at an interface. $\mathcal{I}$ and $\mathcal{R}$ are the interface plane and reflection planes, respectively. Vector $\mathbf{n}$ indicates the normal to the interface $\mathcal{I}$, vector ∇P is parallel to the propagation direction of the incident P-mode. The vector represented by the dashed line indicate the propagation direction of the reflected S-mode, and vector $\mathbf{S}$ shows its polarization direction. ∇P and $\mathbf{n}$ are both contained within the reflection plane $\mathcal{R}$, while $\mathbf{S}$ is orthogonal to plane $\mathcal{R}$.

3 ESTIMATION OF THE REFLECTOR NORMAL

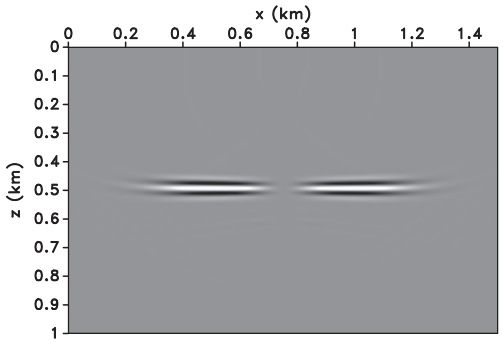
The scalar imaging condition requires an estimate of the reflector normal $\mathbf{n}$. If the velocity is incorrect, reflectors in PP, PS, and SP images are incorrectly positioned, and it is inaccurate to estimate the normal for PS and SP imaging from the PP image. Reflector normals estimated from a PP image are inconsistent with those from a PS image and thus are unavailable for the scalar imaging condition. Therefore, instead of estimating reflector normals from a PP image, we choose to estimate the normal vectors from the PS image computed using the conventional imaging condition. Because the polarity reversal present in conventional PS images results in poor resolution of the stacked conventional PS image, we apply a simple correction for this polarity change, for example, by reversing the sign of the image at negative source-receiver offsets. Alternatively, we could estimate the reflector normal on individual images obtained with the conventional imaging condition that



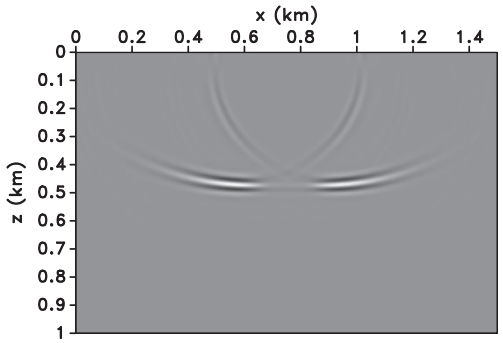
(a)



(b)



(c)



(d)

Figure 2. (a) 2D synthetic model. The dot represent the location of the source and the line represent the location of the receivers. (b) The PP image obtained by crosscorrelating the source and receiver P wavefields. (c) PS and (d) SP images obtained using the scalar imaging condition. Here, the SP image is overlaid by an artifact with moveout. There is no polarity reversal in both images.

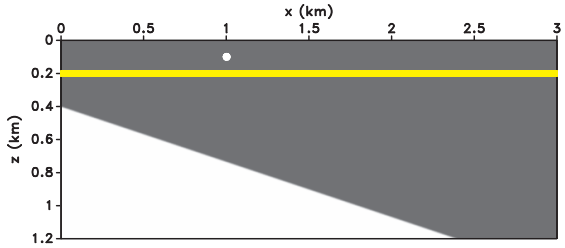
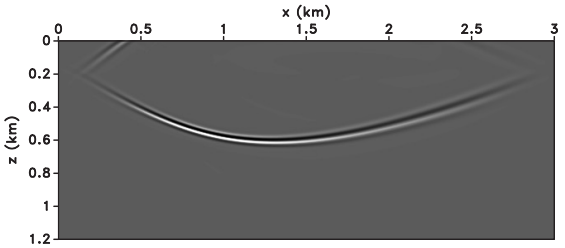
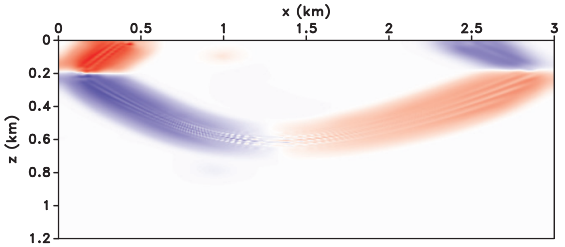


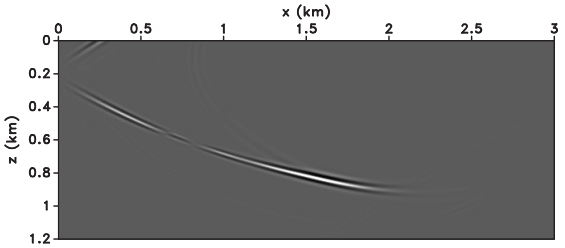
Figure 3. Synthetic model with one dipping reflector. The source, indicated by the dot, is located at $(0.1, 1.0)$ km. The receiver line, indicated by the line, is at $z = 0.2$ km.



(a)



(b)



(c)

Figure 4. (a) The PP image computed by crosscorrelating P-waves in source and receiver wavefields. (b) The reflector normal estimated using the PP image. (c) The PS image computed using the dip field in panel (b). Note that the image of the reflector incorrectly changes polarity at around (0.7,0.6) km.

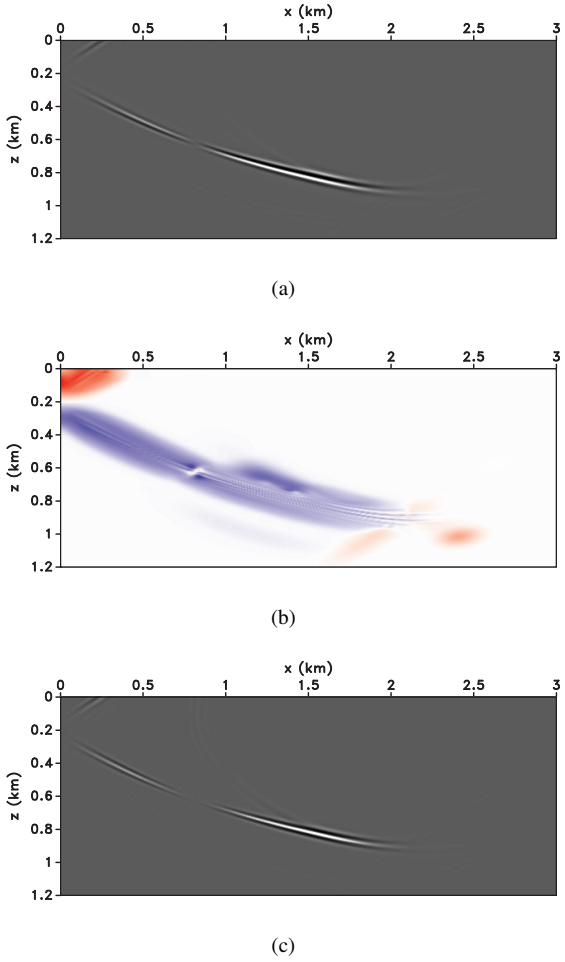


Figure 5. (a) The PS image obtained by crosscorrelating the source P wavefield and receiver S wavefield. (b) The reflector dip estimated using PS image. (c) The PS image computed using the dip field from panel (b). This PS image has no polarity change.

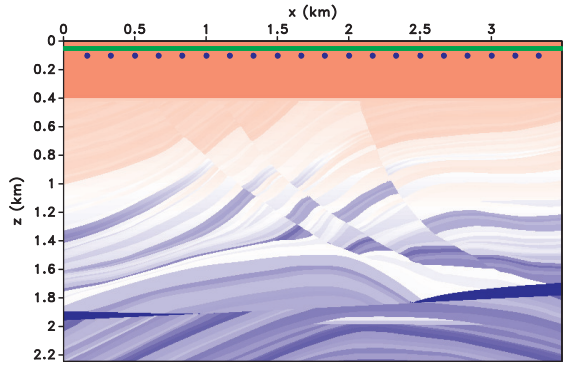


Figure 6. The Marmousi model. The 20 sources, indicated by the dots, are located at depth $z = 0.1$ km. The receiver line, indicated by the line, is at $z = 0.05$ km.

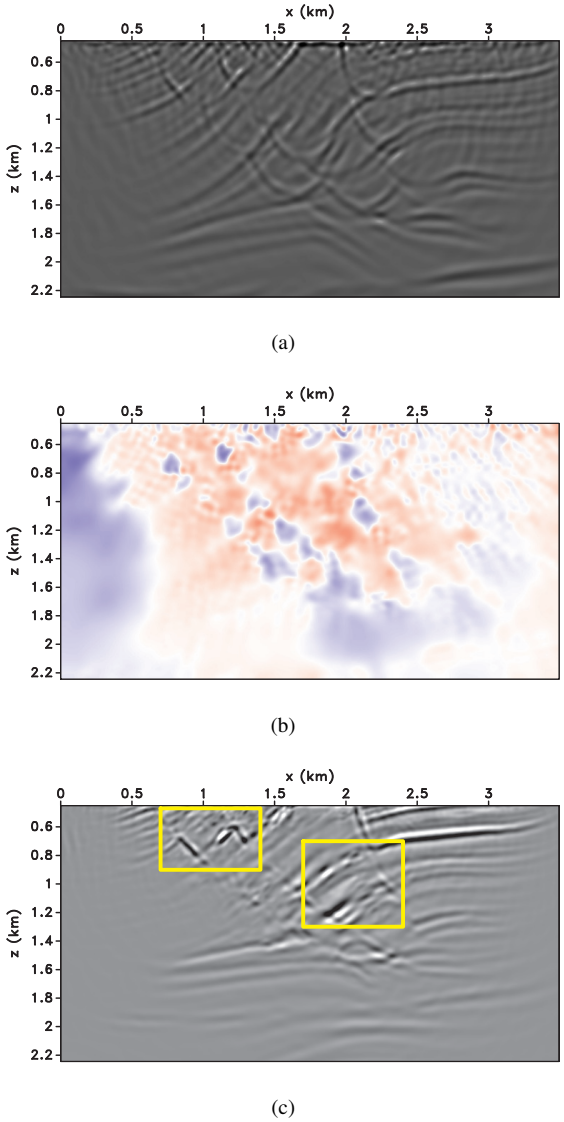


Figure 7. (a) The stacked PP image computed by crosscorrelating P-waves in source and receiver wavefields. (b) The reflector normal estimated using the PP image. (c) The PS image computed using the dip field from panel (b). The reflectors highlighted by the boxes are not continuous and poorly imaged.

does not correct for polarity reversal, at higher overall computational cost.

We demonstrate our approach for estimating reflector normals using a model with a single dipping reflector, Figure 3. We use a displacement source located at $(1.0, 0.1)$ km, and we record the displacement wavefield with a line of receivers at depth $z = 0.2$ km. The source function is a Ricker wavelet with a peak frequency of 30 Hz. The P- and S-wave velocities of the true models are 2.6 and 1.5 km/s, respectively. For migration, we use incorrect constant P- and S-wave velocities of 2.0 and 1.6 km/s, respectively. Note in Figure 4(a) that the reflector in the PP image computed using the incorrect ve-

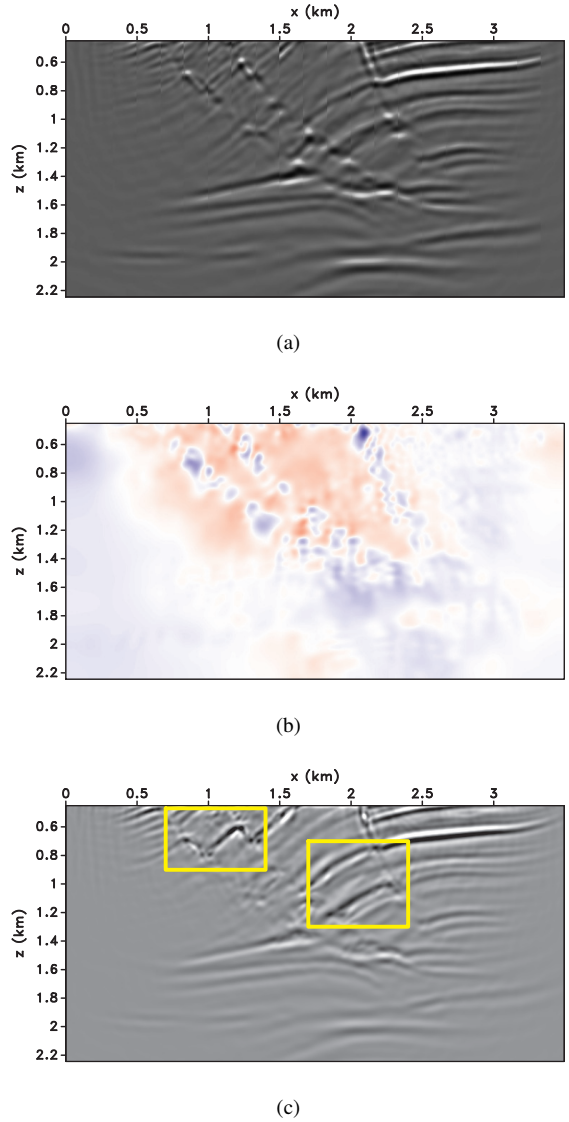


Figure 8. (a) The stacked PS image computed by crosscorrelating P-waves in the source wavefield and S-waves in the receiver wavefield. The PS image polarity for individual shots are corrected by reversing the image at negative offsets. (b) The reflector dip estimated using PS image. (c) The PS image computed using the dip field. The reflectors highlighted by the boxes are better imaged compared to the PS image in Figure 7(c).

locity is located above the position of the true reflector and also incorrectly exhibits curvature. Next, using the estimated normal vectors (Figure 4(b)) from the PP image, we obtain the PS image shown in Figure 4(c). Comparing Figure 4(a) to Figure 4(c), we observe that the position of the reflector in the PP image differs from that of the reflector in the PS image; thus, reflector normals computed from the PP image are not suitable for use in PS migration. This is further demonstrated by the fact that the PS image computed using the reflector normals from Figure 4(b) show polarity reversal at $(0.7, 0.6)$ km. We address this issue by using the conventional PS image (Figure 5(a)), instead of the PP image, to estimate the reflector normal vectors (Figure 5(b)). With the normal vectors shown in Figure 5(b), the resulting PS image shown in Figure 5(c) has no polarity change. The explanation for this behavior is that all vectors used in our imaging condition are consistent with one-another, although they are all distorted by the inaccurate migration velocity.

We illustrate our approach using a modified Marmousi model (Versteeg, 1991, 1993), as shown in Figure 6. Compared with the original model, we increase the depth of the water layer in order to generate PS conversion from a hard water bottom. Twenty explosive sources are evenly distributed along the surface, and 600 multicomponent receivers are located at depth $z = 0.05$ km. The source function is a Ricker wavelet with a peak frequency of 35 Hz. Crosscorrelating the source P wavefield with the receiver P and S wavefields, we obtain the PP (Figure 7(a)) and PS (Figure 8(a)) images, respectively. For the PS image in Figure 8(a), we apply a simple polarity correction by reversing the sign of the pre-stacked PS images at negative source-receiver offsets. Because the P-velocity and S-velocity used for migration are 12% higher and 4% lower than the true model, respectively, the reflectors are at different positions in PP and PS image. With the reflector normal (Figure 7(b)) estimated from the PP image we compute the PS images using the scalar imaging condition (seen in Figure 7(c)). Notice that a reflector changes polarity at $(1.1, 0.7)$ km. If we estimate the reflector normal (Figure 8(b)) using the conventional PS image, we obtain a stacked PS image, computed using the scalar imaging condition, without distortion caused by polarity reversals.

4 IMAGING FROM OPPOSITE SIDES OF A REFLECTOR

In complex subsurface models, reflectors are often illuminated by waves approaching from opposite sides; for example, a reflector might be imaged both from above by a down-going direct wave and from below by a diving wave. Consider the cases shown in Figures 1 and 9, depicting down-going and up-going PS converted waves, respectively. Assuming the incident P-modes in Figures 1 and 9 have the same polarity, then vectors ∇P point in opposite directions, and the reflected S-modes must have opposite polarities because reflectivity changes sign for incident waves approaching a reflector from opposite sides (Aki and Richards, 2002). Therefore, conventional PS images computed by migrating waves reflected off opposite sides of a reflector also have opposite polarities.

In contrast, the polarities of PS images computed using our scalar imaging condition for the two cases shown in Figures 1 and 9 have the same polarity. This is because all reflector normal vectors are defined to point toward only one side of the reflector (the vertical component of all normal vectors must have the same sign in order to avoid ambiguity). Thus, for the same type of incident P-modes, the signs of vector $\nabla P \times \mathbf{n}$ are opposite in the two cases depicted in Figures 1 and 9, because vectors ∇P points in opposite directions. The

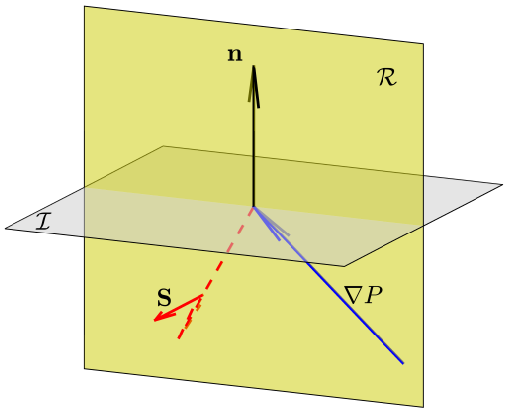


Figure 9. Schematic representation of reflection at an interface for up-going PS converted-modes. Compared to Figure 1, vector ∇P changes sign, resulting in the sign change of $\nabla P \times \mathbf{n}$.

sign change of $\nabla P \times \mathbf{n}$ compensates for the difference in polarity of the reflected S-modes, and results in both SP images having the same polarity regardless of the direction of the incident P-mode. Similarly, for SP images, reflected P-modes on opposite sides of a reflector have different polarities due to the sign change in reflectivity; however, the reflector normal vector $\mathbf{n}$ corrects for the polarity difference in SP images computed from waves reflecting from opposite sides.

To further explain how the scalar imaging condition generates PS images with the same polarity for both cases depicted in Figures 1 and 9, we consider another synthetic example with one horizontal reflector, shown in Figures 10(a)-10(d). The sources and receivers are positioned at the top of the first layer, and the reflector normal points upward. Using the scalar imaging condition, we obtain the PS image shown in Figure 10(a). If we switch the material properties of the top and bottom layers while keeping the acquisition geometry and the direction of the reflector normal vector unchanged, we obtain the PS image shown in Figure 10(b), which has opposite polarity compared to the image in Figure 10(a). Next, if we rotate the entire experiment shown in Figure 10(b) by 180 degrees or, equivalently, reverse the direction of the z-axis, we obtain the PS image shown in Figure 10(c) with the same polarity as the PS image shown in Figure 10(b). Finally, by simply reversing the direction of the reflector normal from Figure 10(c) to Figure 10(d), we obtain the PS image in Figure 10(d) with the same polarity as the image shown in Figure 10(a). Notice that the only difference between the models shown in Figures 10(a) and 10(d) is that the incident P-modes illuminate the horizontal reflector from opposite sides. Therefore, using the scalar imaging condition, we obtain PS images of the same polarity for up-going and down-going waves.

We illustrate migration with waves approaching reflectors from opposite sides using a model consisting of gently dipping layers (Figure 11). The sources and receivers are in two wells. We use 20 sources evenly distributed in the well at $x = 0.1$ km, and 500 receivers located at $x = 1.4$ km. Using the conventional imaging condition, we obtain the PS image shown in the left panel of Figure 12(a). The reflectors around $z = 1.2$ km are poorly imaged because they are illuminated by waves from opposite sides. In the common image gather at $x = 0.8$ km, the right panel of Figure 12(a), the polarities of the events in different experiments are inconsistent. In contrast, Figure 12(b) shows the PS image using the scalar imaging condition. In this case, the interfaces in the image around $x = 1.4$ km are stronger, and the events have consistent polarities in all experiments, which confirms that the PS images computed using waves reflected at opposite sides of the reflector have consistent polarities.

5 CONCLUSIONS

Duan and Sava (2014) propose a scalar imaging condition for converted waves that corrects for polarity reversals in PS and SP images. Additional prior information, i.e., the reflector normal, is required for this imaging condition. In this paper, we discuss two practical problems of the scalar imaging condition. One is the estimation of reflector normals when the reflectors are imaged at incorrect positions. We show that it is more reliable to estimate reflector normals for PS and SP migration from stacked PS and SP images computed using conventional imaging methods. The other problem is imaging a reflector using waves from opposite sides. Using this scalar imaging condition, we obtain converted wave images of consistent polarities when waves are reflected from opposite sides of a reflector.

6 ACKNOWLEDGMENTS

We thank sponsor companies of the Consortium Project on Seismic Inverse Methods for Complex Structures, whose support made this research possible. The reproducible numeric examples in this paper use the Madagascar open-source software package (Fomel et al., 2013) freely available from http://www.ahay.org.

REFERENCES

Aki, K., and P. Richards, 2002, Quantitative seismology (second edition): University Science Books.

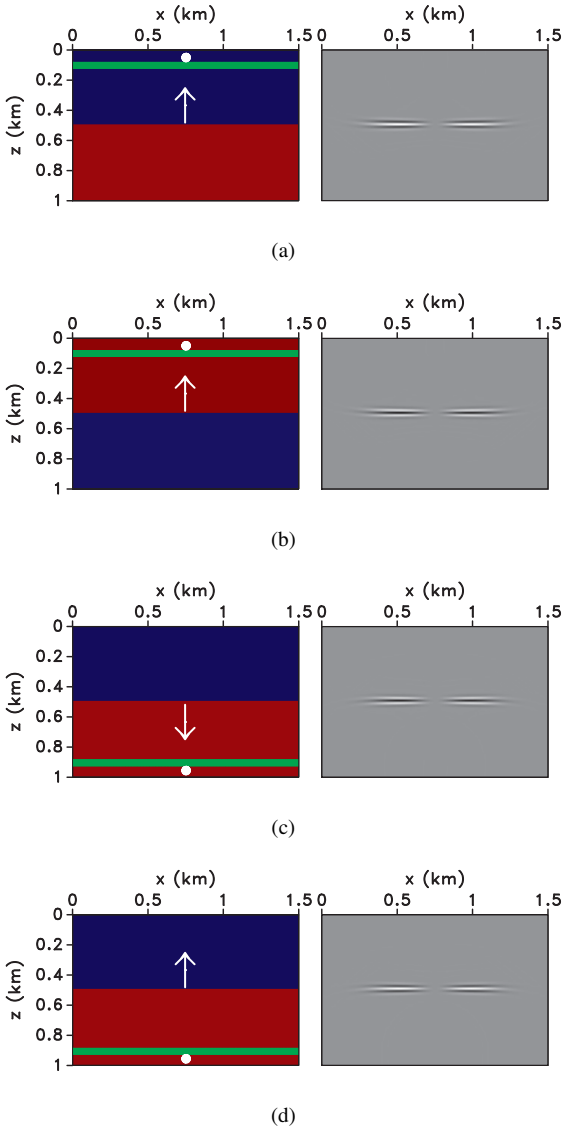


Figure 10. PS imaging of a horizontal interface for various source/receiver configurations. The left panels are the models with the acquisition geometry, and the right panels are the corresponding PS images. The dots are the locations of the sources and lines are the locations of the receivers. The arrow indicates the reflector normal for PS migration. Note that the polarities of the PS images are the same in experiments (a) and (d), but different from experiments (b) and (c).

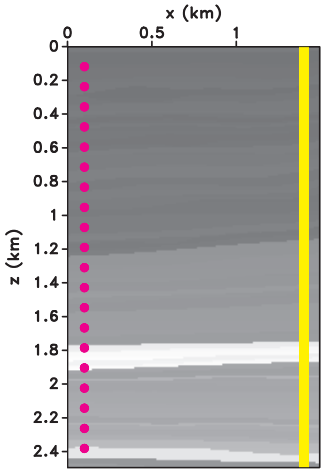


Figure 11. A crosswell example illustrating illumination for opposite sides of a reflector. The 20 sources, indicated by the dots, are in a well at $x = 0.1$ km. The receivers, indicated by the line, are at $x = 1.4$ km.

Artman, B., I. Podladtchikov, and A. Goertz, 2009, Elastic time-reverse modeling imaging conditions: SEG Technical Program Expanded Abstracts 2009, 1207–1211.

Dellinger, J., and J. Etgen, 1990, Wavefield separation in two-dimensional anisotropic media: Geophysicas, **55(7)**, 914–919.

Denli, H., and L. Huang, 2008, Elastic-wave reverse-time migration with a wavefield-separation imaging condition: SEG Technical Program Expanded Abstracts 2008, 2346–2350.

Duan, Y., and P. Sava, 2014, Converted-waves imaging condition for elastic reverse-time migration: SEG Technical Program Expanded Abstracts, 1904–1908.

Fomel, S., P. Sava, I. Vlad, Y. Liu, and V. Bashkardin, 2013, Madagascar: open-source software project for multidimensional data analysis and reproducible computational experiments: Journal of Open Research Software, **1**, e8.

MacLeod, M., R. Hanson, C.R.Bell, and S. McHugo, 1999, The Alba Field Ocean Bottom Cable Seismic Survey: Impact on Development: The Leading Edge, **18**, 1306–1312.

Mehta, K., D. Kiyashchenko, P. Jorgensen, J. Lopez, J. Ferrandis, and A. Mateeva, 2009, Advancements in processing and imaging of downhole multi-component data: SEG Technical Program Expanded Abstracts, 4299–4303.

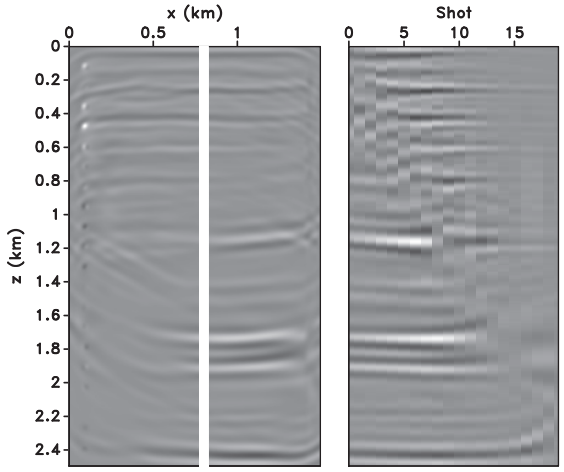
Sen, M. K., 2009, Estimation of properties of shallow sediments from multi-component ocean bottom seismometer data: SEG Technical Program Expanded Abstracts, 4280–4281.

Versteeg, R., 1991, Analysis of the problem of the velocity model determination for seismic imaging: PhD thesis, University of Paris VII.

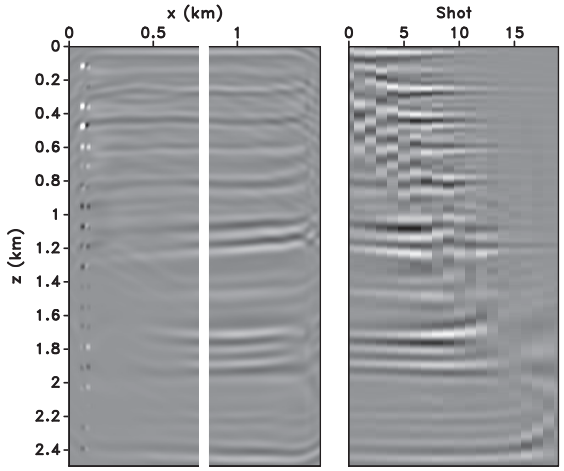
———, 1993, Sensitivity of prestack depth migration to the velocity model: Geophysics, **58**, 873–882.

Wu, R., R. Yan, and X, 2010, Elastic converted-wave path migration for subsalt imaging: SEG Technical Program Expanded Abstracts 2010, 3176–3180.

Yan, J., and P. Sava, 2008, Isotropic angle-domain elastic reverse-time migration: Geophysics, **73(6)**, S229–S239.



(a)



(b)

Figure 12. (a) The stacked PS image using conventional imaging condition. The reflectors around $z = 1.2$ km are not imaged. (b) The stacked PS image using the scalar imaging condition. The reflectors around $z = 1.2$ km are well-imaged. The left panels are the stacked PS images and the right panels are common image gathers at $x = 0.8$ km. Note that for Figure (a), the polarities of the events in the common image gather are inconsistent from left to right, while for Figure (b), the events have consistent polarities in all experiments.